Materialia 25 (2022) 101540

Contents lists available at ScienceDirect

Materialia

journal homepage: www.elsevier.com/locate/mtla

On Σ9 grain boundary plane orientation

Hossein Beladi[a,*], Vahid Tari[b], Gregory S. Rohrer[c]

[a] Institute for Frontier Materials, Deakin University, Geelong, VIC 3216, Australia
[b] ATI Specialty Materials, Monroe, NC 28111, United States
[c] Department of Materials Science and Engineering, Carnegie Mellon University, Pittsburgh, PA 15213-3890, United States

ARTICLE INFO

Keywords:
Σ9 boundary, Σ3 boundary coherency
Boundary plane orientation
Triple junction
Five-parameter boundary characterisation

ABSTRACT

Past measurements of the orientation of the Σ9 grain boundary plane have consistently shown that it adopts a tilt orientation. However, in different circumstances, a wide range of symmetric and asymmetric tilt boundaries are observed. Here, a stereological interpretation of electron-backscatter diffraction data was used to measure the orientation of the Σ9 grain boundary plane in Fe-30Ni. The grain boundary plane orientation was found to be influenced by the types of boundaries meeting the Σ9 at triple points. Σ9 boundaries attached to random high angle boundaries showed a nearly continuous range of symmetric and asymmetric tilt boundaries. Σ9 boundaries attached to Σ3 boundaries selectively adopted a range of lower energy grain boundaries with grain boundary normals between (001) and $(1\bar{1}1)$ orientations. As the coherency of the attached Σ3 boundaries increased, the grain boundary plane orientation maximum was found at the $(1\bar{1}4)//(1\bar{1}4)$ symmetric tilt orientation, thought to be minimum energy for this disorientation. The distribution of Σ9 grain boundary plane orientations depends on the fraction of Σ3 boundaries and how close they are to the coherent twin orientation.

1. Introduction

Grain boundary engineering (GBE) is widely employed to enhance materials performance, specifically for metals with the face centred cubic (FCC) structure. Certain coincidence site lattice (CSL) boundaries display a significant resistance to corrosion and fracture [1–5] and there is increasing evidence that this is related more to the grain boundary plane orientation than to the misorientation [6,7]. The Σ3 boundary is the most abundant CSL boundary in FCC materials with low-to-medium stacking fault energy. When it is coherent (comprised of two parallel (111) planes in the adjoining crystals), it has minimum energy and noticeably contributes to the material performance [2,5,8,9]. Therefore, a considerable body of work was carried out to introduce different approaches (e.g., iterative recrystallization) to enhance the population of Σ3 boundaries [3,4].

CSL boundaries are part of a network in the microstructure and meet at triple lines where there are only two independent misorientations, dictating the third boundary at the triple junction. For instance, if two Σ3 boundaries impinge at a triple junction, the third boundary must be Σ9 (i.e., Σ3 + Σ3 → Σ9) [10]. This interaction is known as twin multiplication in FCC materials, which in general leads to the formation of $\Sigma 3^n$ CSL boundaries [2,3]. Σ9 boundaries are the second most abundant CSL boundary, known as a geometrically necessary component of a twinning based GBE microstructure. It has been demonstrated that they have greater resistance against corrosion compared with general random boundaries [11].

The property of a given boundary depends on its atomic structure/energy, which changes with the boundary plane orientation. Recent technological developments in electron microscopy analysis make it possible to resolve the grain boundary plane orientations for a given grain boundary type, through the stereological analysis of electron backscatter diffraction data [12]. This method was broadly employed to measure the grain boundary plane orientations for different grain boundary types in a wide range of materials [5,13–17]. It has been found that the shape of the grain boundary plane distribution is consistent for materials with the same crystal structure and the relative areas are inversely proportional to the relative grain boundary energies [18]. However, the Σ9 boundary has been an exception to both of these trends, despite being characterized by a similar approach [5,8,9,11,16,17]. For example, while the majority of Σ9 boundaries have tilt character, the distribution of grain boundary plane orientations in the [110] zone differs in different materials. In addition, while the minimum energy Σ9 tilt boundary in Ni and other FCC metals is the {411} symmetric tilt grain boundary (STGB) [19], this is seldom a unique maximum in the distribution. In fact, in some cases local maxima are also observed at the relatively high energy {221} STGB [17]. Despite a significant body of work on grain boundary characterisation, the diverse boundary plane distributions reported for the Σ9 boundary in FCC materials is poorly

* Corresponding author.
E-mail address: hossein.beladi@deakin.edu.au (H. Beladi).

https://doi.org/10.1016/j.mtla.2022.101540
Received 19 May 2022; Accepted 6 August 2022
Available online 7 August 2022

understood. One unique characteristic of the Σ9 boundary is that it is frequently connected to coherent Σ3 boundaries, and this creates constraints on the grain boundary plane orientation. We explore here the hypothesis that, for Σ9 boundaries, the grain boundary plane orientation depends on the boundaries to which it is connected at triple junctions. The results indicate that the coherency of connected Σ3 boundaries influences the distribution of Σ9 grain boundary planes.

2. Experimental procedure

The material used in the current study was fully austenitic with a composition of Ni-29.5Fe-0.01C-0.02Mn (in wt.%). The as-received material was in the form of a billet with a thickness of 40 mm. It was initially subjected to multiple rolling passes in a temperature range of 1200–1000 °C to reduce the thickness to ~ 20 mm. The material was then machined to produce a torsion sample with a gauge length and a diameter of 20 mm and 6.7 mm, respectively. The material was subjected to thermomechanical processing using a torsion rig, described in detail elsewhere [20]. The sample was primarily reheated to 1200 °C and isothermally held for 80 s to homogenise the temperature throughout the sample. It was then subjected to two deformation steps at an equal strain of 0.4 at a strain rate of 1 s^{-1}. Each deformation was followed by a 40 s isothermal hold to fully recrystallise the microstructure. Afterwards, the sample was immediately water-quenched, resulting in an equiaxed grain structure.

Electron backscatter diffraction (EBSD) mapping was used to determine the microstructure of a tangential section of the specimen at a depth of ~ 100 μm beneath the surface of the gauge length. EBSD samples were prepared through standard mechanical polishing routines followed by a colloidal silica slurry polish. A FEI Quanta 3D FEG SEM/FIB instrument was employed to acquire multiple EBSD maps, operating at 20 kV and 8 nA current. The BESD data acquisition and post-processing were conducted using the TexSEM Laboratories (TSL) software. The EBSD maps were obtained at a step size of 1 μm on hexagonal grid, covering ~ 62.7 mm^2 (590 μm × 590 μm × 180 maps). The average confidence index was ~ 0.82. To characterise the five-parameter grain boundary character distribution, a series of EBSD data post-processing routines were conducted using TSL software. At first, ambiguous data were removed using a grain dilation clean-up function. Afterwards, a single orientation was assigned to each grain by averaging all orientations belonging to that grain. The grain boundary traces on the surface were approximated by straight line segments that did not deviate from the observed boundary position by more than 2 pixels (i.e., 2 μm) using the reconstruct grain boundary function in the TSL software. Therefore, the smoothing process converted a curved boundary to more than one boundary line trace/segment. In total, ~ 303,000 boundary line segments/traces were collected. These line traces were used to compute the five-parameter grain boundary character distribution through an automated stereological approach, which described in detail elsewhere [12]. As described in more detail in [21], although observations from plane sections by themselves do not provide information about the inclination of the grain boundary plane for a single boundary, the stereological analysis of a large number of observations provides a reliable estimate of the distribution of grain boundary plane orientations. It should be emphasised that the current five-parameter approach offers 8° resolution to measure the grain boundary plane of Σ9 (i.e., ideal Σ9 misorientation, 38.9°/<110>), which is greater than 5° angular deviation by Brandon criterion [22].

3. Results and discussion

The microstructure consisted of fully recrystallised equiaxed grains with an average size of 49 ± 1 μm (Fig. 1a). The misorientation angle distribution exhibited a prominent peak at the position of 60° (Fig. 1b). The misorientation axis vectors related to 60° rotation angle were strongly clustered about the ⟨111⟩ direction. This shows that the first-order Σ3 twin boundaries, characterised by the 60°/<111> misorientation, make up a substantial fraction of the high-angle boundaries (~ 53.3%), consistent with the Σ3 twin boundaries observed in the microstructure (Fig. 1a). There was also a small peak at ~ 39° with a misorientation axis centred at the ⟨101⟩ direction. This represents the second-order Σ9 twin boundaries characterised by the 39°/<101> misorientation (Fig. 1b). The fraction of Σ9 twin boundaries was ~ 3.5%. Not all Σ9 boundaries were connected to Σ3 boundaries. They were either isolated or

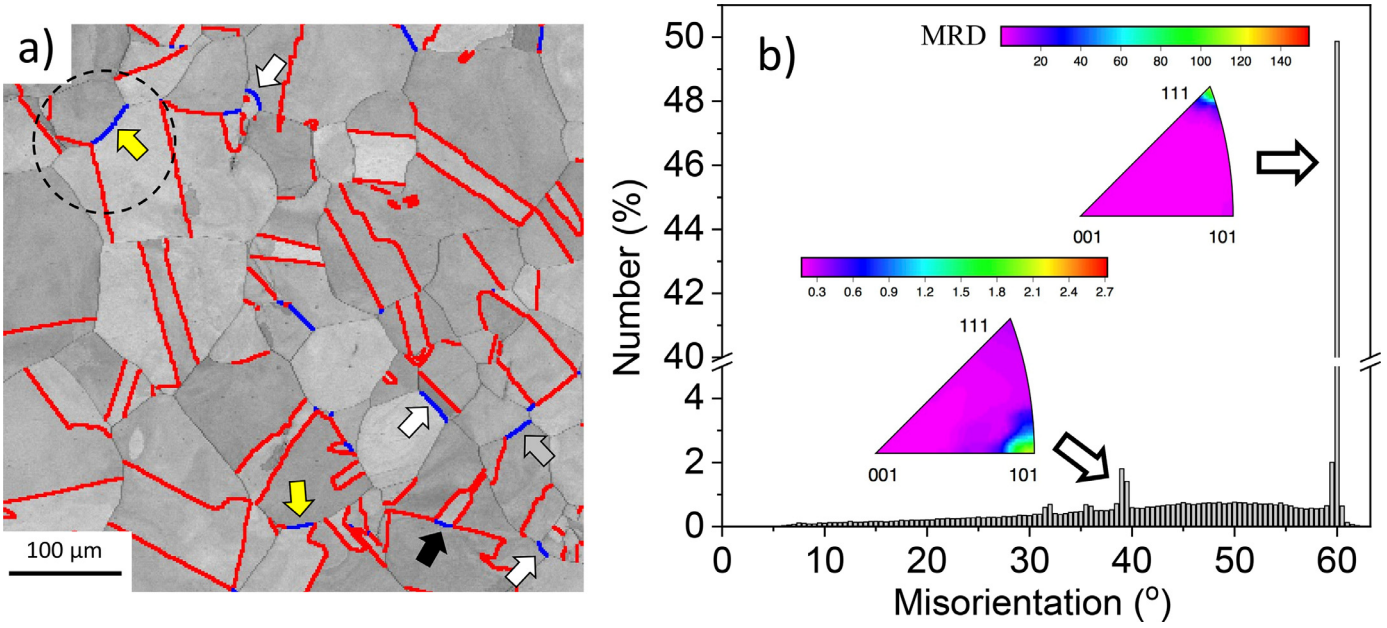

Fig. 1. (a) the band contrast EBSD image of Ni-30Fe alloy. Red and blue lines in (a) are Σ3 and Σ9 boundaries, respectively. White, light grey, yellow and black arrows in (a) represent triple junctions, containing a Σ9 connected to none, one, two and four Σ3 boundaries, respectively. (b) misorientation angle distribution along with the distribution of axes at rotation angles of 60° and 39° in a standard stereographic triangle for Ni-30Fe alloy. MRD is multiples of a random distribution.

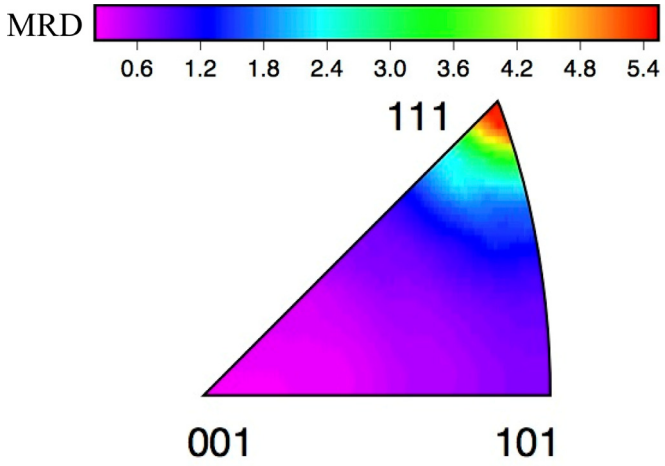

Fig. 2. Grain boundary plane distribution for all boundaries, irrespective of misorientation, of Ni-30Fe alloy. MRD represents multiples of a random distribution.

connected to one, two or four Σ3 boundaries at the triple junction/s (Fig. 1a).

The relative areas of grain boundary planes independent of misorientation drawn in the crystal reference frame (Fig. 2) exhibited a strong anisotropy having a maximum at the (111) orientation with ~ 5.6 MRD (multiples of a random distribution). This emphasises that the (111) plane area was ~ 460% greater than expected in a random distribution. The minimum appeared at (001) position with ~ 0.23 MRD and the intensity of (101) orientation was ~ 1 MRD. This is consistent with earlier reports and is consistent with the idea that {111} planes in FCC materials have relatively low grain boundary energies, leading to their population enhancement in the microstructure [8,9].

The Σ3 grain boundary plane distribution exhibited a maximum at the orientation of the (111)//(111) pure twist boundary (Fig. 3a). This matches the orientation of the minimum energy Σ3 boundary measured and calculated in FCC materials [6,7,19,23,24]. The Σ9 grain boundary plane distribution revealed maxima along the [110] zone, comprising multiple positions (Fig. 3b). This suggests that these boundaries have symmetrical and asymmetrical tilt characters. The main peak appeared at $(1\bar{1}4)//(1\bar{1}4)$ symmetrical tilt position, spreading towards $(001)//(1\bar{1}\bar{2})$ and $(1\bar{1}1)//(\bar{1}1\bar{5})$ planes. Interestingly, a local minimum was also observed at $(\bar{2}21)//(\bar{2}21)$ along the [110] zone (Fig. 3b). The observation of multiple local maxima along the [110] zone is qualitatively consistent with previously reported observations, but the orientation with the maximum population is not the same in all of the studies [5,8,9,11,16,17].

Grain boundary energies are inversely correlated to the grain boundary relative areas so we expect to see the maximum in the distribution at the minimum energy [18]. Because grain boundary energies for Ni-30Fe are not available in the literature, the grain boundary energies for Ni computed by Olmsted et al. [19] are employed in the current study. While it is recognized that these energies will not be identical to those of the Ni alloy, it has been reported that the energies of metals with the FCC structure obey a scaling relation [25], suggesting that the shape of the distribution will be comparable. Therefore, the grain boundary energies of Ni will be used as a proxy for the grain boundary energies of the Ni-30Fe alloy. Here, grain boundary energies for Ni were plotted in the same reference frame as the grain boundary plane distribution in Fig. 3c. The calculations indicate that the lowest energies occur along the zone of tilt boundaries and be minimum energy is found at $(1\bar{1}4)//(1\bar{1}4)$ STGB orientation, consistent with the experimental observations. There are other boundaries with relatively low energies along the tilt axis from $(\bar{1}15)//(1\bar{1}\bar{1})$, to $(001)//(1\bar{1}\bar{2})$, and $(1\bar{1}1)//(\bar{1}1\bar{5})$. The current grain boundary area results correlate well with the calculated energies. The reason the maximum population extends along the axis of tilt grain boundaries is that the energies of the $(1\bar{1}4)//(1\bar{1}4)$ STGB and the different asymmetric tilt grain boundaries (such as $(1\bar{1}1)//(\bar{1}1\bar{5})$) have competitive energies that differ by less than 5%. Using the functional dependence of the Σ9 grain boundary energy specified in [26], the energies ($\gamma_{\Sigma 9}(\phi)$) and torques ($\frac{\partial \gamma_{\Sigma 9}(\phi)}{\partial \phi}$) associated with tilt boundaries are illustrated in Fig. 4. Note that none of the boundaries are singular and the grain boundary energies exceed the torques by a factor of roughly five. In other words, the energy landscape is relatively flat along the zone of Σ9 tilt grain boundaries.

One might hypothesize that the discrepancies in reported grain boundary plane orientations for FCC metals results from different processing routes or alloy compositions. However, the previously studied alloys were largely produced through processes similar to the current study, consisting of normal nucleation and growth (i.e., recrystallization), which leads to a boundary network with the minimum energy arrangement. The alloy composition influences the stacking fault energy of alloy and/or the grain boundary energy and composition. The former largely affects the population of Σ3 boundaries rather their orientation [2]. The change in the composition of grain boundary directly influences its energy, either through segregation or by changing the grain boundary complexion (grain boundary phase) [27]. This might, in turn,

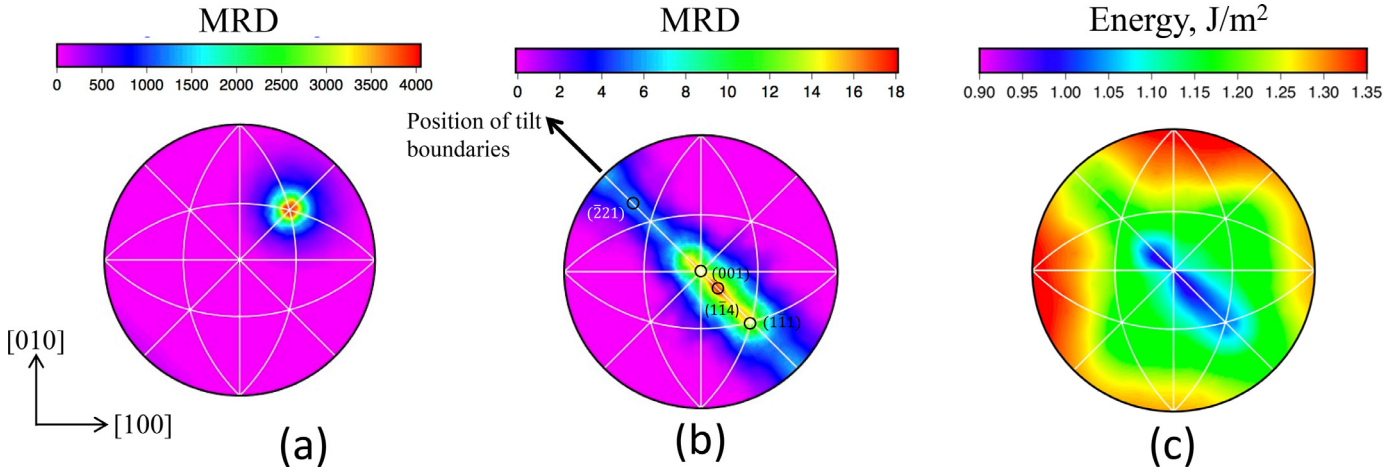

Fig. 3. The distribution of plane normals for (a) Σ3 boundaries and (b) Σ9 boundaries in Ni-30Fe alloy. (C) the grain boundary energy distribution for Σ9 boundaries computed in Ni [19]. MRD represents multiples of a random distribution.

Table 1
Number and length fractions of coherent and incoherent Σ3 boundaries for different deviation angles from (111) plane.

Deviation angle from (111), °	Number Fraction (Total Σ3: 37.23 ± 0.11%)		Length Fraction (Total Σ3: 53.29 ± 0.01%)	
	Coherent Σ3 (%)	Incoherent Σ3 (%)	Coherent Σ3 (%)	Incoherent Σ3 (%)
3	14.42 ± 0.23	22.80 ± 0.23	27.11 ± 0.16	26.17 ± 0.16
5	19.50 ± 0.21	17.73 ± 0.21	36.25 ± 0.17	17.03 ± 0.17
10	24.73 ± 0.09	12.50 ± 0.09	45.07 ± 0.05	8.22 ± 0.05

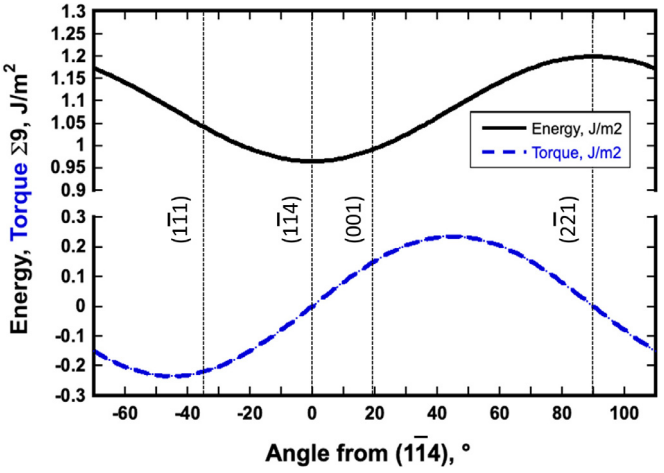

Fig. 4. The energies of Σ9 grain boundaries along the zone of tilt boundaries, referenced to the orientation of the (1$\bar{1}$4) STGB. Several low index orientations are marked for reference. The grain boundary torques, or differentials with respect to the angle, are shown by the dashed line. Based on the results in [26].

alter the grain boundary plane orientation. However, it is worth mentioning that the multiple plane orientations for Σ9 were also reported in pure Ni, where there are no deliberately added alloys to segregate [8]. Therefore, there are no obvious connections between the reported differences in Σ9 grain boundary plane distribution and the composition or processing.

To test the hypothesis that Σ9 grain boundary plane orientation is related to the coherency of the Σ3 boundaries, the Σ3 boundaries were classified into two categories, coherent and incoherent boundaries based on the angular deviation from the ideal {111} planes. In other words, the Σ3 boundaries with the grain boundary trace orientation within the angular deviation from the trace expected for the ideal {111} twin plane orientation were considered coherent Σ3 boundaries in the current study. As thresholds to separate the two Σ3 categories, we used angular deviations of 10°, 5°, and 3°, the latter of which is the estimated to be the maximum resolution of the experiment. This estimate arises from the minimum angle (α) that can be measured between vectors on a discrete grid with spacing (Δ) and vector (grain boundary) length (L), which is $\sin\alpha = \Delta/L$. The grid spacing is 1 μm and, assuming a typical boundary length is 40% of the grain radius ($L = 20$ μm), the resolution is estimated to be about 3°. The deviation angle threshold significantly influenced both the number fraction and length fraction of Σ3 coherent and incoherent boundaries. In general, the number fraction and length fraction of Σ3 incoherent boundaries increased with tightening the deviation angle at the expense of Σ3 coherent boundaries. For example, the length fraction of coherent Σ3 boundaries progressively increased from 27.1 ± 0.1% to 45.1 ± 0.1% as the deviation angle from the ideal {111} increased from 3° to 10°, respectively (Table 1).

In addition, it was necessary to classify the triple points into categories. Using four types of grain boundaries (random (R), Σ9, Incoherent Σ3, and Coherent Σ3), there are 13 possible categories, as listed in Table 2. The number of junctions in each of these categories depends on the deviation angle threshold that separates coherent from incoherent Σ3. For example, at a 10° deviation angle, the highest number fraction of triple junction belonged to two random boundaries (i.e., R) connected to coherent Σ3 boundary (~48.5%, Table 2). As the deviation angle tightened, the number fraction of coherent Σ3-R-R triple junctions progressively reduced, reaching to ~ 31% at a 3° deviation angle.

Table 2
Triple junction classification based on different types of boundaries, namely coherent Σ3 and incoherent Σ3, Σ9 and random (R) boundaries. Coherent Σ3 and incoherent Σ3 boundaries were differentiated considering different deviation angles from (111) plane.

Triple Junction Classification	Number Fraction (%)		
	3° deviation	5° deviation	10° deviation
R-R-R	20.8 ± 0.1	20.8 ± 0.1	20.8 ± 0.1
Coherent Σ3-R-R	31.0 ± 0.5	40.2 ± 0.4	48.5 ± 0.2
Incoherent Σ3-R-R	26.7 ± 0.5	17.4 ± 0.4	9.2 ± 0.1
Coherent Σ3-Coherent Σ3-Σ9	1.85 ± 0.06	3.27 ± 0.08	5.29 ± 0.07
Incoherent Σ3-Incoherent Σ3-Σ9	3.10 ± 0.10	1.70 ± 0.10	0.60 ± 0.02
Coherent Σ3-Incoherent Σ3- Σ9	4.90 ± 0.10	4.90 ± 0.10	4.95 ± 0.06
Coherent Σ3-Incoherent Σ3-R	2.03 ± 0.05	2.48 ± 0.05	2.61 ± 0.05
Coherent Σ3-Coherent Σ3-R	0.16 ± 0.01	0.35 ± 0.02	0.78 ± 0.03
Incoherent Σ3-Incoherent Σ3-R	1.66 ± 0.05	1.03 ± 0.04	0.47 ± 0.02
Σ9-R-R	3.74 ± 0.04	3.74 ± 0.04	3.74 ± 0.04
Σ9-Σ9-R	0.10 ± 0.01	0.10 ± 0.01	0.10 ± 0.01
Incoherent Σ3-Σ9-R	2.00 ± 0.05	1.38 ± 0.04	0.76 ± 0.02
Coherent Σ3-Σ9-R	2.00 ± 0.05	2.60 ± 0.05	3.20 ± 0.05

For the analysis of the Σ9 grain boundary planes, we focused on Σ9 boundaries in four types of junctions, as illustrated schematically in Fig. 5.

- Type I: Isolated triple junction, where Σ9 boundary is connected to random (R) boundaries at the triple junction/s, Σ9-R-R.
- Type II: Incoherent Σ3-Incoherent Σ3-Σ9 triple junction/s,
- Type III: Coherent Σ3-Incoherent Σ3-Σ9 triple junction/s,
- Type IV: Coherent Σ3-Coherent Σ3- Σ9 triple junction/s,

It is worth mentioning that a curved grain boundary is converted to several boundary segments through a smoothing process in the current study. Therefore, a given Σ9 curved boundary can be classified in different triple junction categories from either side (see dash circle in Fig. 1a). As expected, the number of Σ9 boundaries in each triple junction category was affected significantly by the degree of Σ3 coherency. As the deviation angle from the {111} increased, the number of coherent Σ3-coherent Σ3-Σ9 triple junctions increased at the expense of other triple junction categories. The five-parameter analysis approach requires approximately 2000 boundary line segments/traces of a specific disorientation to reliably measure its grain boundary plane distribution [12]. Therefore, the distribution was not plotted for conditions in which the number of Σ9 boundaries became less than 2000 boundary line segments after the filtering process. For this reason, the distribution of grain boundary planes is not plotted for the type IV junctions when the threshold angle for coherent Σ3 boundaries was less than 5°

The distributions in Fig. 6 are relative areas. Because of the filtering operations, it is not meaningful to compute the relative area in units of

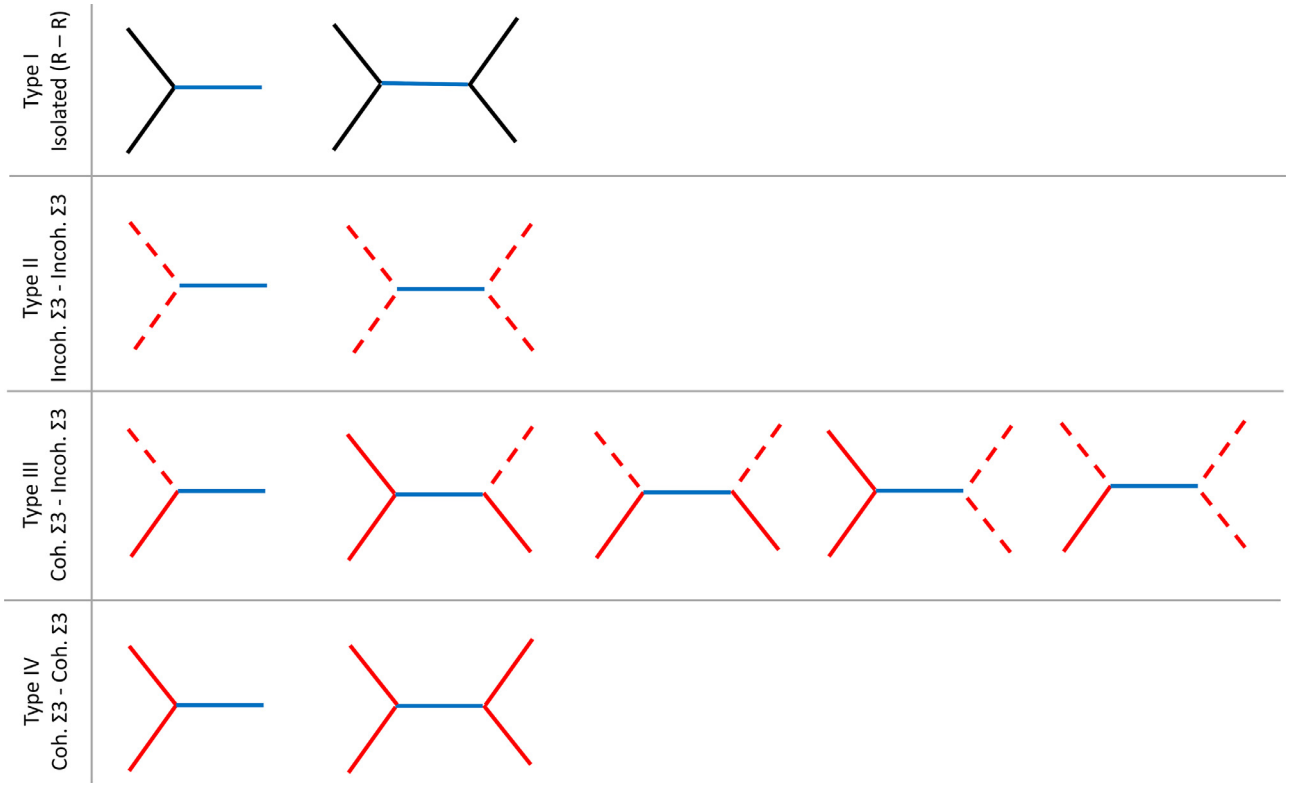

Fig. 5. Schematic representation of different triple junction types/arrangements containing Σ9 boundary. Black, red, dash red and blue lines represent random, coherent Σ3, incoherent Σ3 and Σ9 boundaries, respectively. R, Coh. and Incoh. are random, coherent Σ3 and incoherent Σ3 boundaries, respectively.

MRD. Instead, the distributions of relative areas are normalized to have a maximum of 1. Note also that there is a mirror plane perpendicular to [110] coincident with the zone of tilt boundaries. While most of the intensity is on the tilt axis, boundaries that are not pure tilt will create some intensity on both sides of the axis. For the triple junction type I, where Σ9 is connected to two random boundaries, the distribution exhibits a uniform spread of intensity along the zone of tilt boundary positions, showing all possible tilt boundaries with symmetric and asymmetric characters (Fig. 6a). Note that this is distinct from the distribution illustrated in Fig. 3b, which had most of the boundaries at inclinations with low energies between $(1\bar{1}1)$ and $(\bar{1}15)$. This distribution is qualitatively similar to Σ9 boundaries connected to incoherent Σ3-incoherent Σ3 boundaries at triple junctions considering a 10° deviation angle from the ideal {111} (Fig. 6b). For these boundaries, all tilt boundaries have similar high relative areas, not correlated to the details of the calculated energies, as illustrated in Fig. 4.

For Σ9 boundaries at type III triple junction, i.e., connected to coherent Σ3-incoherent Σ3 boundaries, the intensity is spread between two strong peaks at the (001) and $(1\bar{1}1)$ tilt boundary positions, considering 10° deviation angle threshold from the ideal {111} (Fig. 6a). With a decrease in the deviation angle threshold, the (001) and $(1\bar{1}1)$ peaks progressively merged, leading to the appearance of a single strong peak at $(1\bar{1}4)//(1\bar{1}4)$ position (Fig. 6f,g). This is qualitatively similar to the distribution observed for Σ9 boundaries type IV triple junction, i.e., connected to two coherent Σ3 boundaries, displaying a single peak at the position of $(1\bar{1}4)//(1\bar{1}4)$ symmetric tilt position, which became more pronounced with a decrease in the coherency tolerance angle from 10° to 5° (Fig. 6h, i).

The selection of the grain boundary plane at a triple junction is dictated by the Herring condition [28]:

$$\gamma_i \vec{t}_i + \frac{\partial \gamma_i}{\partial \phi} \vec{n}_i = 0$$

The Herring condition is a summation over forces tangential ($\vec{t}_i$) and normal ($\vec{n}_i$) to the three interfaces and γ_i is the energy of the i^{th} interface. This is illustrated in Fig. 7 for the special junction containing the Σ9 $(1\bar{1}4)//(1\bar{1}4)$ boundary meeting the two coherent twins. Here, the dihedral angles are fixed by the geometry: $\Psi_{\Sigma 9}$=70.53° and $\Psi_{\Sigma 3}$=144.7°. This is dictated by the symmetry of the situation, because the two Σ3 boundaries are identical, the Σ9 must be on the symmetric plane between them. If we ignore the torque terms, the Herring equation reduces to $\gamma_{\Sigma 9}=2\gamma_{\Sigma 3}\cos(\Psi_{\Sigma 9}/2)$. Based on the energies computed by Olmsted et al. [19], $\gamma_{\Sigma 9}$=0.95 J/m^2, $\gamma_{\Sigma 3}$=0.06 J/m^2, and $2\gamma_{\Sigma 3}\cos(\Psi_{\Sigma 9}/2)$ = 0.098 J/m^2, which is about one tenth of $\gamma_{\Sigma 9}$. Therefore, it must be the torque forces associated with the Σ3 boundary that stabilize the junction.

The coherent twin boundary is singular [29], which also means that the torque forces are ill-defined at this orientation. However, one can pose the question, how large must the torques be to stabilize this configuration? Again, referring to Herring equation [28], the force balance is

$$\gamma_{\Sigma 9} = 2\gamma_{\Sigma 3} cos\left(\frac{\Psi_{\Sigma 9}}{2}\right) + 2\frac{\partial \gamma_i}{\partial \phi} cos\left(\frac{\pi}{2} - \frac{\Psi_{\Sigma 9}}{2}\right)$$

This leads to the result that $\frac{\partial \gamma_i}{\partial \phi} \geq 0.74$ J/m^2. While it is not possible to know the torque for the singular boundary, we can estimate a minimum value. Recognizing that the grain boundary energy of Ni increases by about 1 J/m^2 as one rotates by Π/2 radians from [111] to $[\bar{1}10]$, a minimal estimate of the torque is defined by this slope, which is 0.64 J/m^2. Because this minimum estimate of the torque associated with the coherent twin is similar the torque needed to stabilize the symmetric configuration, we conclude that the grain boundary torque is a plausible force to stabilize the symmetric junction.

When the Σ9 meets boundaries at triple lines that are not singular, then the dihedral angles must adjust accordingly. Because of the relative flat energy landscape and weak torque forces (see Fig. 4), the Σ9

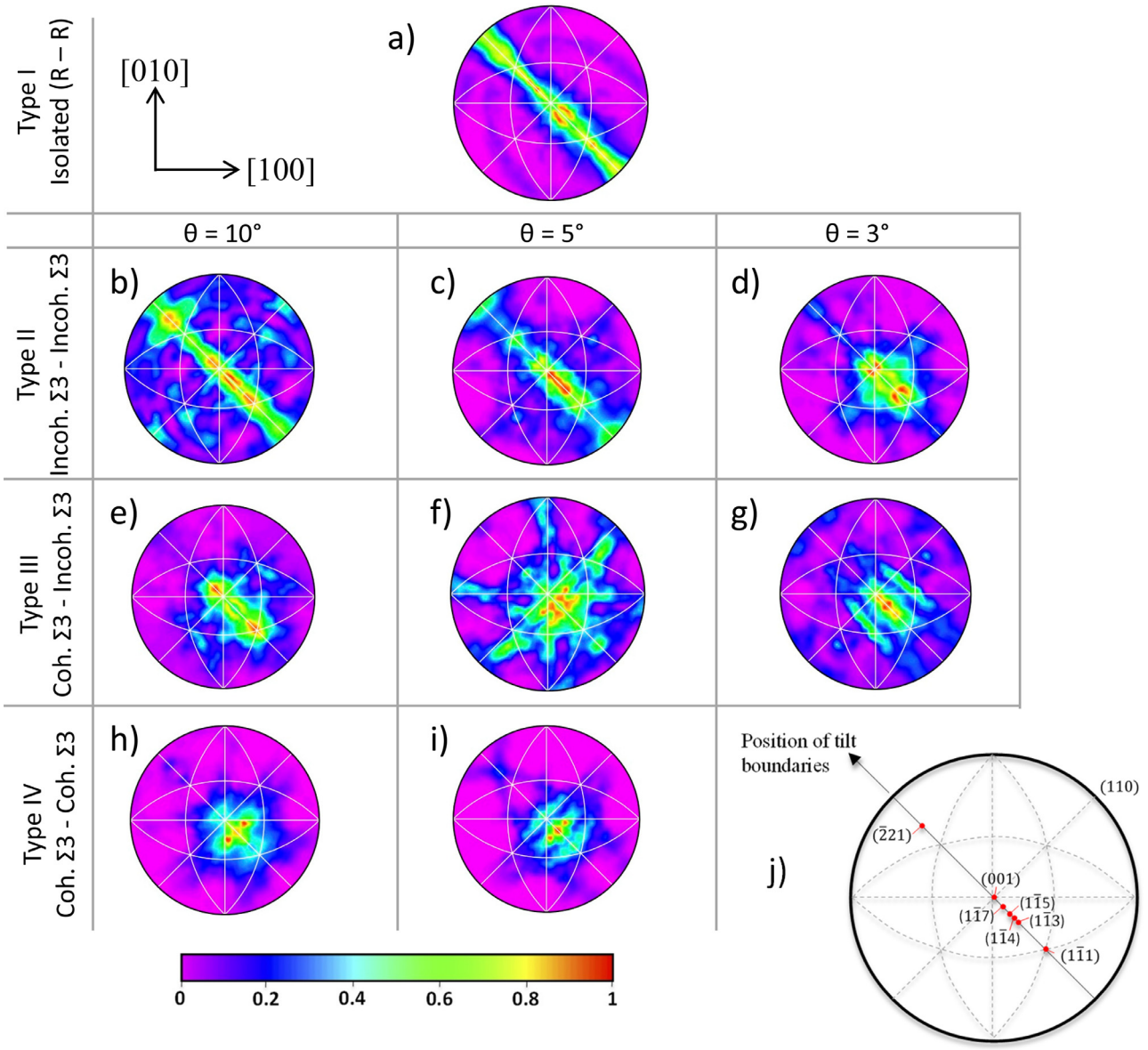

Fig. 6. (a through i) The distribution of relative areas for different types of Σ9 boundaries in Ni-30Fe alloy, considering different triple junction classifications in terms of random, coherent Σ3 and incoherent Σ3 boundaries arrangements. R, Coh, Incoh, θ and MRD are random, coherent Σ3 and incoherent Σ3 boundaries, the deviation angle of Σ3 boundary from {111} and multiples of a random distribution, respectively. (j) schematic representation of [110] tilt boundary plane positions.

boundary plane is free to adopt other orientations as needed to satisfy the Herring condition. This is a plausible explanation for the dependence of the grain boundary plane orientation on the triple junction type and suggests that the details of the Σ9 grain boundary plane orientation distribution will depend on the fraction of coherent twin boundaries in the material.

The current analysis clearly demonstrates that the grain boundary plane distribution of Σ9 is geometrically constrained by the characteristics of Σ3 boundaries at the triple junction. The impingement of two ideal coherent Σ3 boundaries at the triple junction leads to the formation of $(1\bar{1}4)//(1\bar{1}4)$ symmetric tilt Σ9 boundary, which is the minimum energy arrangement [23,24,30] (Figs. 6 and 7). However, if the Σ3 boundaries are not coherent, the Σ9 boundary can adopt asymmetric grain boundary plane orientations to satisfy the Herring condition, but do not necessarily represent the minimum energy Σ9 boundary orientation. The extent of change in the Σ9 plane orientation depends on the cumulative deviation of the Σ3 boundaries from the ideal coherent orientation. Therefore, the extent of Σ3 coherency in the microstructure largely dictates the grain boundary plane distribution of the Σ9 boundary.

4. Conclusion

The Σ9 boundary grain boundary plane distribution was measured in a Fe-30Ni alloy as a function of Σ3 coherency using the five-parameter grain boundary characterisation approach. It was shown that the Σ9 boundary plane orientation was influenced by the degree of Σ3 coherency. A Σ9 boundary connected to two ideal coherent Σ3 boundaries at triple junctions exhibited a $(1\bar{1}4)//(1\bar{1}4)$ symmetric tilt grain boundary orientation, which is presumably the minimum energy arrangement. For boundaries other than coherent Σ3 boundaries, the Σ9 boundary can adopt a range of orientations in the [110] zone, which has a relatively flat energy landscape. Although these other orientations are not

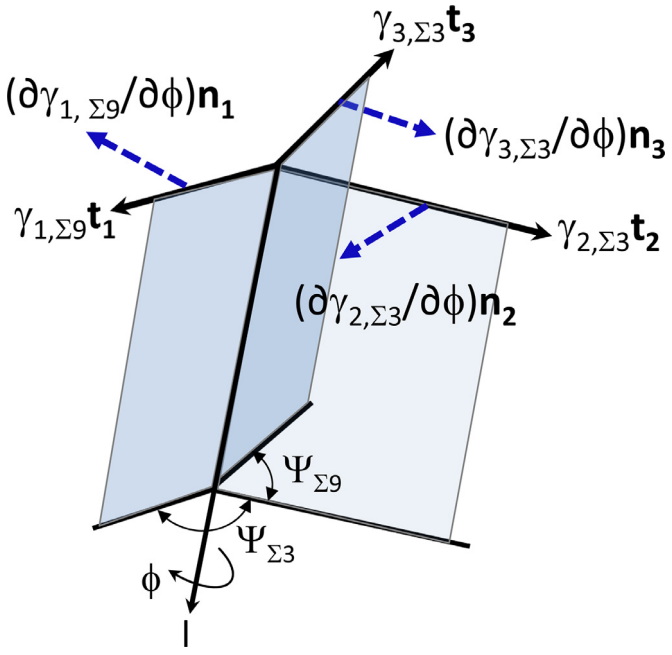

Fig. 7. Schematic of a triple junction, assuming a junction between two coherent twins and a symmetric Σ9 $(1\bar{1}4)//(1\bar{1}4)$ boundary. The symbols are defined in the text.

the minimum energy Σ9 orientation, they presumably satisfy the Herring condition at the triple junction.

Declaration of Competing Interest

The authors declare that they have no known competing financial interests or personal relationships that could have appeared to influence the work reported in this paper.

Acknowledgements

Deakin University's Advanced Characterization Facility is acknowledged for use of the EBSD instruments.

References

[1] T. Watanabe, The impact of grain boundary character distribution on fracture in polycrystals, Mater. Sci. Eng. A 176 (1994) 39–49, doi:10.1016/0921-5093(94)90957-1.
[2] V. Randle, Mechanism of twinning-induced grain boundary engineering in low stacking-fault energy materials, Acta Mater. 47 (1999) 4187–4196, doi:10.1016/S1359-6454(99)00277-3.
[3] V. Randle, A. Brown, Development of grain misorientation texture, in terms of coincident site lattice structures, as a function of thermomechanical treatments, Philos. Mag. 59 (1989) 1075–1089, doi:10.1080/01418618908209838.
[4] A.J. Schwartz, The potential engineering of grain boundaries through thermomechanical processing, JOM 50 (1998) 50–55, doi:10.1007/s11837-998-0250-5.
[5] G.S. Rohrer, V. Randle, C.-.S. Kim, Y. Hu, Changes in the five-parameter grain boundary character distribution in α-brass brought about by iterative thermomechanical processing, Acta Mater. 54 (2006) 4489–4502, doi:10.1016/j.actamat.2006.05.035.
[6] D. An, T.A. Griffiths, P. Konijnenberg, S. Mandal, Z. Wang, S. Zaefferer, Correlating the five parameter boundary character distribution and the intergranular corrosion behaviour of a stainless steel using 3D orientation microscopy based on mechanical polishing serial sectioning, Acta Mater. 156 (2018) 297–309, doi:10.1016/j.actamat.2018.06.044.
[7] C.S. Kim, A.D. Rollett, G.S. Rohrer, Grain boundary planes: new dimensions in the grain boundary character distribution, Scr. Mater. 54 (2006) 1005–1009, doi:10.1016/j.scriptamat.2005.11.071.
[8] J. Li, S.J. Dillon, G.S. Rohrer, Relative grain boundary area and energy distributions in nickel, Acta Mater. 57 (2009) 4304–4311, doi:10.1016/j.actamat.2009.06.004.
[9] H. Beladi, N.T. Nuhfer, G.S. Rohrer, The five parameter grain boundary character and energy distributions in a fully austenitic high manganese steel using three dimensional data, Acta Mater. 70 (2014) 281–289, doi:10.1016/j.actamat.2014.02.038.
[10] K. Miyazawa, Y. Iwasaki, K. Ito, Y. Ishida, Combination rule of Sigma values at triple junctions in cubic polycrystals, Acta Crystallogr. 52 (1996) 787–796, doi:10.1107/S0108767396005934.
[11] V. Randle, M. Coleman, M. Waterton, The role of Σ9 boundaries in grain boundary engineering, Metall. Mater. Trans. A 42 (2011) 582–586, doi:10.1007/s11661-010-0302-7.
[12] G.S. Rohrer, D.M. Saylor, B.E. Dasher, B.L. Adams, A.D. Rollett, P. Wynblatt, The distribution of internal interfaces in polycrystals, Z. Met. 95 (2004) 197–214, doi:10.3139/146.017934.
[13] H. Beladi, Q. Chao, G.S. Rohrer, Variant selection and intervariant crystallographic planes distribution in martensite in a Ti-6Al-4V alloy, Acta Mater. 80 (2014) 478–489, doi:10.1016/j.actamat.2014.06.064.
[14] H. Beladi, G.S. Rohrer, A.D. Rollett, V. Tari, P.D. Hodgson, The distribution of intervariant crystallographic planes in a lath martensite using five macroscopic parameters, Acta Mater. 63 (2014) 86–98, doi:10.1016/j.actamat.2013.10.010.
[15] H. Beladi, A. Ghaderi, G.S. Rohrer, Five-parameter grain boundary characterization of randomly textured AZ31 Mg alloy, Philos. Mag. 100 (2020) 456–466, doi:10.1080/14786435.2019.1692154.
[16] H. Beladi, P. Cizek, A. Taylor, G.S. Rohrer, P.D. Hodgson, Static Softening in a Ni-30Fe austenitic model alloy after hot deformation: microstructure and texture Evolution, Metall. Mater. Trans. A 48 (2017) 855–867, doi:10.1007/s11661-016-3880-1.
[17] M. Laleh, A.E. Hughes, M.Y. Tan, G.S. Rohrer, S. Primig, N. Haghdadi, Grain boundary character distribution in an additively manufactured austenitic stainless steel, Scr. Mater. 192 (2021) 115–119, doi:10.1016/j.scriptamat.2020.10.018.
[18] G.S. Rohrer, Grain boundary energy anisotropy: a review, J. Mater. Sci. 46 (2011) 5881–5895, doi:10.1007/s10853-011-5677-3.
[19] D.L. Olmsted, S.M. Foiles, E.A. Holm, Survey of computed grain boundary properties in face-centered cubic metals: I. Grain boundary energy, Acta Mater. 57 (2009) 3694–3703, doi:10.1016/j.actamat.2009.04.007.
[20] H. Beladi, G.L. Kelly, P.D. Hodgson, The effect of multiple deformations on the formation of ultrafine grained steels, Metall. Mater. Trans. A 38 (2007) 450–463, doi:10.1007/s11661-006-9080-7.
[21] D.M. Saylor, B.S. El-dasher, B.L. Adams, G.S. Rohrer, Measuring the five-parameter grain boundary distribution from observations of planar sections, Metall. Mater. Trans. A 35 (2004) 1981–1989, doi:10.1007/s11661-004-0147-z.
[22] D.G. Brandon, The structure of high-angle grain boundaries, Acta Metall. 14 (1966) 1479–1484, doi:10.1016/0001-6160(66)90168-4.
[23] N. Gokon, M. Kajihara, Experimental determination of boundary energies of Σ9 [110]asymmetric tilt boundaries in Cu, Mater. Sci. Eng. A 477 (2008) 121–128, doi:10.1016/j.msea.2007.05.029.
[24] K.L. Merkle, D. Wolf, Low energy configurations of symmetric and asymmetric tilt grain boundaries, Philos. Mag. A 65 (1992) 513–530, doi:10.1080/01418619208201536.
[25] E.A. Holm, D.L. Olmsted, S.M. Foiles, Comparing grain boundary energies in face-centered cubic metals: Al, Au, Cu and Ni, Scr. Mater. 63 (2010) 905–908, doi:10.1016/j.scriptamat.2010.06.040.
[26] R.M. Moore, T. Beecroft, G.S. Rohrer, C.M. Barr, E.R. Homer, K. Hattar, B.L. Boyce, F. Abdeljawad, The grain boundary stiffness and its impact on equilibrium shapes and boundary migration: analysis of the Σ5, 7, 9, and 11 boundaries in Ni, Acta Mater. 218 (2021) 117220, doi:10.1016/j.actamat.2021.117220.
[27] P.R. Cantwell, M. Tang, S.J. Dillon, J. Luo, G.S. Rohrer, M.P. Harmer, Grain boundary complexions, Acta Mater. 62 (2014) 1–48, doi:10.1016/j.actamat.2013.07.037.
[28] C. Herring, W.E. Kingston, Surface tension as a motivation for sintering, in: The Physics of Powder Metallurgy, McGraw-Hill, New York, 1951, p. 36.
[29] F. Abdeljawad, S.M. Foiles, A.P. Moore, A.R. Hinkle, C.M. Barr, N.M. Heckman, K. Hattar, B.L. Boyce, The role of the interface stiffness tensor on grain boundary dynamics, Acta Mater. 158 (2018) 440–453, doi:10.1016/j.actamat.2018.06.025.
[30] S.L. Thomas, A.H. King, D.J. Srolovitz, When twins collide: twin junctions in nanocrystalline nickel, Acta Mater. 113 (2016) 301–310, doi:10.1016/j.actamat.2016.04.030.